

The impact of photospheric brightness field on exoplanetary transit timings and the TTV excess of HD 189733 *b*

Roman V. Baluev^{*}

Saint Petersburg State University, 7–9 Universitetskaya Emb., Saint Petersburg 199034, Russia

Accepted 2021 October 20. Received 2021 October 18; in original form 2021 September 17

ABSTRACT

We consider the issue of excessive TTV noise observed for the exoplanet HD 189733 *b*. Trying to explain it through the host star photospheric activity, we model the stellar surface brightness as a random field, then characterize statistical properties of the resulting transit signal perturbation and compute individual corrections to transit timings uncertainties. We find that possible effect of the photospheric brightness field can explain only a minor portion (~ 10 s) of the observed (~ 70 s) TTV excess of HD 189733, suggesting that the rest should be attributed to other sources. Regarding the photospheric pattern, we place an upper limit of ~ 0.01 on the combination $\varepsilon_{\text{cell}} r_{\text{cell}}$, where $\varepsilon_{\text{cell}}$ is the relative magnitude of brightness variations, and r_{cell} is the geometric cellularity scale (relative to star radius).

Key words: planetary systems - techniques: photometric - stars: activity - stars: individual: HD 189733 - methods: data analysis - methods: statistical

1 INTRODUCTION

Transit timing variations, or TTVs, appear if the Keplerian motion of a transiting exoplanet is somehow perturbed. The sources of such a perturbation can be different. For example, it can come from another body in the system, so the TTVs can be considered as an additional method of exoplanet detection (Holman & Murray 2005; Agol et al. 2005). Previously, this approach allowed to detect a statistically sound list of exoplanets from the NASA *Kepler* mission (Ford et al. 2011; Steffen et al. 2013; Xie 2013).

Alternatively, long-term TTV trends may appear because of a tidal interaction between the planet and its host star, so that planet can exhibit either a slow spiral falling on the star or a long-period apsidal drift. Such an example is provided by the planet WASP-12 (Maciejewski et al. 2016, 2018; Bailey & Goodman 2019). Yet another example of this kind, though less certain, is provided by WASP-4 (Bouma et al. 2019; Baluev et al. 2020). But later it appeared that its TTV trend can be due to a long-term secular acceleration revealed in radial velocity (Bouma et al. 2020).

The present work is devoted, in general, to further advance of the TTV method, and, in particular, to further development of the EXPANSION project (EXoPlanetary trANsit Search with an International Observational Network). EXPANSION is a ground-based TTV project, grown on the basis of the Exoplanet Transit Database (Baluev et al. 2015; Sokov et al. 2018; Baluev et al. 2019,

2020, 2021). It involves an international network of several dozens of rather small-aperture amateur and professional telescopes, aimed to monitor exoplanetary transits. The network comprises observatories that are spreaded over the world in the both hemispheres.

Baluev et al. (2015, 2019) presented TTV analysis of large sets of exoplanetary transit lightcurves from the EXPANSION project. In these works an important issue was revealed concerning the accuracy of the derived timing measurements. While some targets demonstrated good agreement of their TTV noise with the estimated timing uncertainties, others revealed an obvious TTV excess. However, that TTV excess could not be explained through a simple deterministic model (like a TTV trend or a periodic variation). It looked like a random noise, though with a considerably larger magnitude than one should expect from the derived uncertainties. It does not seem that there is a clear separation between TTV-stable and TTV-noisy stars, but the most prominent example of the second type is HD 189733 *b*. Its TTV noise is roughly twice as large as expected, and in absolute magnitude the TTV excess is above 1 min. This appears paradoxical, because for HD 189733 many accurate high-quality lightcurves are available, for which such level of timing noise is well above reasonable fitting errors. Baluev et al. (2019) hypothesized that TTV excesses observed for HD 189733 and some other EXPANSION targets might be related to stellar activity.

HD 189733 is indeed known for a strong activity, as confirmed by multiple observation campaigns (Boisse et al. 2009; Cauley et al. 2017; Pillitteri et al. 2014). Therefore,

^{*} E-mail: r.baluev@spbu.ru

this star suits well as a test case to deeply investigate the TTV noise excess and its possible cause.

Star spots and star faculae are the most obvious activity manifestation capable to distort apparent exoplanetary transit times. See e.g. (Montalto et al. 2014), and an expanded review of the issue in (Baluev et al. 2021). The latter work presents an attempt of a systematic search of all statistically detectable spot-crossing events in a big photometric data base. Although about a hundred of such potential events were detected, this comprised just a few per cent of all transit lightcurves analysed. No obvious correlation was revealed between the target TTV excess and the number of detected spot- and facula-crossing events. Therefore, they cannot offer an easy explanation of the issue.

Although explicitly *fittable* spots/faculae events are rare, there may be a larger number of smaller spots or activity regions in the star photosphere that cannot be fitted individually, or even detected, but can excite a significant perturbation to the transit signal. Yet another phenomenon with a similar effect is photospheric granulation that can impose a significant distortion on the fitted transit parameters (Chiavassa et al. 2017). In both these cases the transit curve perturbation acts as if the photometry involved an additional noisy signal. Such a perturbation cannot be predicted for an individual transit, but it can be treated statistically, as a random process.

Of course, all contemporary transit fitting techniques and software involve a dedicated and adaptive model of the photometric noise. In particular, they should routinely take into account an adjustable noise level and possibly correlated (red) noise. However, such methods are always model-dependent at some level, and there is no guarantee that we adequately fit all types of the activity-induced photometric signals. Hence, some unforeseen biases may appear in the timings, and this can be precisely that effect revealed in HD 189733 and other TTV-noisy targets.

In this work we undertake an attempt to test this hypothesis with HD 189733 transit data. Since there are multiple physical phenomena that can excite photospheric structures to be obscured by a transiting planet, we avoid assuming any particular physical mechanism for them. Instead of that, we consider the star photosphere as a more or less general random field. Then we try to derive what statistical characteristics of this random field should affect the best fitting transit parameters. This formal view would be somewhat similar to Chiavassa et al. (2017), but with a special emphasis on the transit timings rather than depth. Our goals are to (i) verify whether this approach can explain the TTV excess of HD 189733 and in what part, (ii) derive some numeric statistical characteristics of the stellar photosphere as implied by such treatment or, at least, place relevant numeric limits, (iii) develop more or less practical methods and models that could be used in future work based on this treatment.

The paper therefore assumes the following scheme:

- (i) First of all, we give a more detailed discussion of the TTV noise excess in HD 189733 (Sect. 2).
- (ii) We specify the statistical model of the Photospheric Brightness Field (PBF) (Sect. 3).
- (iii) We determine statistical properties of a photometric transit perturbation generated by the PBF (Sect. 4).

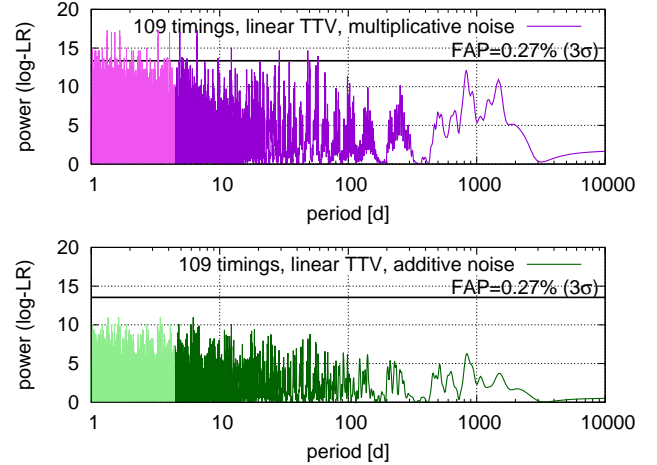


Figure 1. Likelihood-based periodograms of 109 HD 189733 timings from (Baluev et al. 2019), for the first two fits from Table 1. The ordinate is the logarithm of the likelihood ratio for best fits with and without sinusoidal signal. The significance threshold is derived using (Baluev 2008) treatment. The Nyquist range is shown, in each graph, with a darker color. The light-color range is a replica of this primary one, based on periodogram periodic properties.

(iv) We explain the resulting statistical effect on the best fitting parameters of the transit, in particular on the fitted midtimes (Sect. 5).

(v) Given this TTV noise model, we solve the inverse problem, i.e. based on the transit times available for HD 189733 try to determine statistical properties of the PBF necessary to explain such observed timings (Sect. 6).

2 THE ISSUE OF TTV EXCESS IN HD 189733

Baluev et al. (2019) presented a homogeneous analysis of 109 transit lightcurves for HD 189733, involving professional as well as amateur observations from the EXPANSION network. It was noticed that derived transit timing measurements demonstrate an unusually high level of TTV noise than expected from the uncertainties. First of all, let us provide some additional details of this phenomenon.

To assess the effect of TTV noise excess, we computed a maximum-likelihood fit of these 109 timings using linear model for the timings τ_i . We used two alternative TTV noise models that treat transit timing uncertainties $\sigma_{\tau,i}$ differently. The first model is the so-called multiplicative one, in which noise variance expressed as $\mathbb{D}\tau_i = \kappa^2 \sigma_{\tau,i}^2$, with fittable κ . This model corresponds to the classic least-square fit, when the free scale factor κ is often implicit and has the meaning of the reduced χ^2 of the residuals. The second model is the so-called additive one, with $\mathbb{D}\tau_i = \sigma_{\text{jitter}}^2 + \sigma_{\tau,i}^2$, where σ_{jitter} is a fittable ‘jitter’ parameter. More details on these formal models and their discussion are given in (Baluev 2015). The maximum-likelihood fitting method was basically the same as in (Baluev 2009).

The results of these two TTV fits are given in Table 1 (its first block). We can see that the noise scale factor exceeds 2, and this can be alternatively explained through a TTV jitter of ~ 70 s.

Table 1. Comparative properties of several TTV fits for HD 189733.

TTV noise model	Goodness-of-fit \tilde{l} [s] ¹	noise factor κ , equiv. of reduced $\sqrt{\chi^2_r}$	TTV jitter σ_{jit} [s]	Periodogram peak power
All 109 transit timings from (Baluev et al. 2019):				
Multiplicative	92.14	2.11 ± 0.15	0	17.3
Additive	87.96	$\simeq 1$ by construction	67.8 ± 6.8	11.0
Selected 42 lightcurves, reprocessed in this work:				
Multiplicative	101.15	2.69 ± 0.29	0	24.1
Additive	102.66	$\simeq 1$ by construction	82 ± 12	17.0
109 minus five Kasper et al. (2019) lightcurves of 2016-Aug-02:				
Multiplicative	74.32	1.67 ± 0.12	0	8.9
Additive	79.38	$\simeq 1$ by construction	53.1 ± 6.2	7.5
42 minus five Kasper et al. (2019) lightcurves of 2016-Aug-02:				
Multiplicative	59.88	1.54 ± 0.18	0	4.6
Additive	75.35	$\simeq 1$ by construction	23.2 ± 6.0	12.0

¹ A dimensional goodness-of-fit measure directly related to the likelihood, see (Baluev 2009).

Can this TTV noise excess be explained through deterministic variation? As in (Baluev et al. 2019), a possible quadratic TTV trend does not appear statistically significant with any noise model, as it cannot provide a remarkable likelihood improvement. However, the residual periodogram (using linear TTV model as the base) appears puzzling in the case of multiplicative model (Fig. 1). We can see multiple peaks with formal significance above the three-sigma level, but the periodogram still looks more like noise, because there are no clearly dominating isolated periods. Therefore, the excessive TTV variance cannot be convincingly explained through a simple regular variation, looking more like an additional random component.

For HD 189733 multiple amateur transit lightcurves analysed in (Baluev et al. 2019) involved uncertainties or even errors regarding their metadata (e.g. whether the BJD correction was applied or not), or about spectral bandpass (e.g. amateur filters are not always obviously related with the standard astrophysical photometric systems). Although all such uncertainties were apparently resolved in (Baluev et al. 2019), in this work we aimed to perform a possibly cleanest analysis. So in our primary analysis we decided not to rely on the EXPANSION network at all, using only photometric data published in the literature: Bakos et al. (2006), Winn et al. (2007)¹, the HST photometry acquired by Pont et al. (2007) and McCullough et al. (2014), and high-accuracy broadband photometry by Kasper et al. (2019). This builded up 42 transit lightcurves in total.

We applied essentially the same analysis pipeline to them as in (Baluev et al. 2019), which is based on the `transitfit` command of our PLANETPACK software (Baluev 2013a, 2018). Namely, we fit all lightcurves using the same values for planet/star radii ratio, transit duration, impact parameter. Only the midtimes were allowed to vary separately. Also, the lightcurves models included individual cubic trends, and quadratic limb darkening law with coefficients depending on the bandpass.

In this work we fit the limb darkening coefficients only for the HST and T10APT data. The other lightcurves refer

Table 2. Limb darkening coefficients of HD 189733, for different bandpasses.

Band	A	B
Theoretic ¹ from (Claret & Bloemen 2011):		
B	0.839	0.004
V	0.636	0.133
u	1.050	-0.198
g	0.763	0.060
r (same set for R_C)	0.547	0.175
i (same set for I, I_C)	0.436	0.192
z	0.361	0.202
T10APT $b + y$ (not used ²)	0.712	0.103
Fitted in this work:		
HST ACS	0.730 ± 0.034	-0.228 ± 0.047
HST WFC3	0.326 ± 0.094	-0.04 ± 0.12
T10APT $b + y$	0.77 ± 0.16	-0.11 ± 0.20

¹To these theoretic values we further added empiric corrections $\Delta A = 0.004$ and $\Delta B = -0.099$ from (Baluev et al. 2019).²Computed simply as half sum for the b and y bands, but this might appear inaccurate.

to standard photometric filters, so we used theoretically predicted values based on Claret & Bloemen (2011) FCM tables, taking $T_{\text{eff}} = 5109K$, $\log g = 4.69$, $[Fe/H] = 0.03$ from Santos et al. (2013). These theoretic coefficients are listed in Table 2, and they appear close to those used in (Kasper et al. 2019). Notice that we additionally corrected these values by a small systematic bias derived in (Baluev et al. 2019).

The pipeline also involved the red noise detection and fitting algorithm described in details in (Baluev et al. 2019).

The spot-crossing anomalies detection algorithm from (Baluev et al. 2021) was not applied here, because after removal of the EXPANSION lightcurves only the HST photometry was left with formally significant anomalies, but they looked, in turn, like some detrending inaccuracies rather than physical spot-crossing events (see graphs in Baluev et al. 2021). Besides, one of the HST transits turns ill fitted with such a model, if the transit midtimes are allowed to vary.

The resulting set of transit times is shown in Fig. 2. We can see that some points significantly deviate from the linear TTV ephemeris, in particular the group of five timings in 2016 that belong to Kasper et al. (2019). They actually refer to a single transit observed in five filters simultaneously.

¹ Notice that published T10APT photometry revealed double HJD correction, and we used correct data kindly provided by the authors.

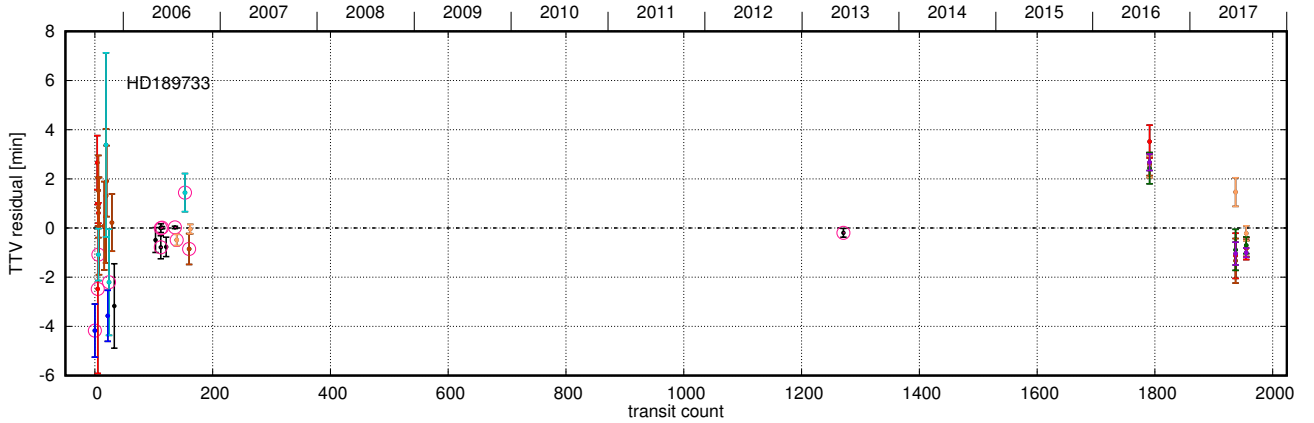


Figure 2. Transit timing residuals obtained for 42 lightcurves of HD 189733 included in the analysis. The color of a point identifies the photometric spectral band (same convention as in [Baluev et al. 2019](#)). Encircled points are those a correlated photometric noise was revealed.

The fits of these selected 42 timings is given in the second block of Table 1. We can see that the TTV noise excess remains there and is even increased. Now both TTV models generate periodograms with unusually boosted noise level without clear dominating peak. This indicates that neither of two models provides a satisfactory statistical explanation of the TTV noise.

We noticed previously that such periodogram behaviour may appear for data with outliers. In view of that we tried to detect possibly odd lightcurves using an analogue of the leave-one-out method. We sequentially removed a single point from our 42 timings, then recomputed the periodogram for this reduced set, and looked how much the periodogram global maximum is changed. As could be expected from Fig. 2, the periodogram is sensitive to the transit observed by ([Kasper et al. 2019](#)) on 2016-Aug-02. By removing these five lightcurves, the TTV fits are significantly improved and the maximum periodogram power falls below reasonable significance thresholds.

However, such treatment remains unsatisfactory. As seen from Table 1 (third and fourth blocks), the TTV noise excess is reduced indeed, but it still persists and remains significant, so the issue is not resolved completely. On the other hand, there is no reasonable explanation why the high-quality [Kasper et al. \(2019\)](#) observations could involve that large errors. Also, two other transits from [Kasper et al. \(2019\)](#) do not indicate so big timing deviation, even though one of them had only partial coverage.

Possible pipeline imperfections may result in systematically undervalued uncertainties, but this effect cannot provide a convincing explanation of the issue. For example, after per-transit averaging our timing estimates are in good agreement with those given by [Kasper et al. \(2019\)](#). Besides, [Baluev et al. \(2019\)](#) verified their timing uncertainties for WASP-12, by comparing them with those obtained by ([Maciejewski et al. 2016, 2018](#)) from the same lightcurves but using alternative analysis. It appeared that [Baluev et al. \(2019\)](#) timing uncertainties may be possibly undervalued by the factor of 1.22. It is difficult to perform a similar comparison for HD 189733, because its data are not so homogeneous as for WASP-12, but we can expect a similar pipeline-

related effect in its τ_i uncertainties as well. Clearly, this is much smaller than the observed TTV effect. Also, there are multiple targets in ([Baluev et al. 2019](#)) that demonstrate a good agreement of their TTV noise with the derived timing uncertainties. If the issue was because of pipeline biases, it would affect either all targets at once or primarily those with poor-quality data (not HD 189733).

Therefore, we should deal with another explanation of the issue, namely that the observed TTV noise of HD 189733 is owed to some physical effect in the star-planet system. Then we should not remove the deviating [Kasper et al. \(2019\)](#) transit, because it may carry the most important information about the effect. The magnitude of the extra TTV noise remains then ~ 80 s, corresponding to $\sim 15\%$ of the planet radius. In this work we try to explain this TTV noise through possible photospheric brightness variations of unspecified nature.

Our two TTV noise models appear statistically similar in terms of their goodness-of-fit, for example the Vuong test ([Vuong 1989; Baluev 2012](#)) indicates, at most, an 1.8-sigma significance for their difference. The additive noise model does not appear clearly better, so our effect in question does not necessarily behave as a constant additional noise. For example, it may affect different timings differently, so we need a nontrivial statistical model for this putative effect.

3 MODEL OF PHOTOSPHERIC BRIGHTNESS FIELD

Let the brightness of star photosphere at the sky-projected position \mathbf{x} be $I(\mathbf{x})$, with $x = 0$ at the projected star center. We treat this $I(\mathbf{x})$ as a random field characterized by some correlation function. Geometrically the photosphere is a sphere, and in the general case there is a projection effect that makes the correlation function (i) spatially nonstationary, and (ii) anisotropic. However, near the star center we can neglect the projection effect and consider the local correlation function k_I :

$$k_I(\mathbf{x} - \mathbf{x}') = \text{Cov}(I(\mathbf{x}), I(\mathbf{x}')) = \mathbb{E}(\delta I(\mathbf{x})\delta I(\mathbf{x}')),$$

$$\delta I(\mathbf{x}) = I(\mathbf{x}) - \mathbb{E}I(\mathbf{x}), \quad \mathbf{x}, \mathbf{x}' \ll R_*. \quad (1)$$

We assume that $k_I(\mathbf{r})$ in (1) is stationary (shift-invariable) and so it depends on just a single argument. We also assume that it is radially symmetric, i.e. it can be rewritten as $k_I(r)$ with a scalar argument r . The spherical geometry distorts both these properties in a mathematically predictable way, but at the local level we may start from such a k_I . In this work we do not address possible effects of an intrinsic (non-projectional) anisotropy of the brightness field, and also we do not consider possible temporal variations in $I(\mathbf{x})$.

Based on the Wiener-Khinchin theorem, we can construct the two-dimensional spatial power spectrum $P_I(s)$, which is also radially symmetric:

$$P_I(s) = \frac{1}{4\pi^2} \int_{\mathbb{R}^2} k_I(\mathbf{r}) e^{i\mathbf{s}\cdot\mathbf{r}} d\mathbf{r} = \frac{1}{2\pi} \int_0^{+\infty} k_I(r) J_0(sr) r dr. \quad (2)$$

The total power is then

$$k_I(0) = \int_{\mathbb{R}^2} P_I(\mathbf{s}) d\mathbf{s}, \quad (3)$$

which appears equal to the variance $\text{Var } I(\mathbf{x})$ and is constant in stationary approximation.

Notice that $I(\mathbf{x})$ may often have a *cellular* structure, i.e. it may remain nearly constant within small geometric units, or cells, in which the correlation keeps high. Therefore, $k_I(0)$ has the meaning of spatial brightness variation between such independent cells. To highlight this, we define $\sigma_{\text{cell}}^2 = k_I(0)$.

In addition to $k_I(0)$, an x -space parameter, let us consider $P_I(0)$, being an analogous s -space characteristic:

$$P_I(0) = \frac{1}{4\pi^2} \int_{\mathbb{R}^2} k_I(\mathbf{r}) d\mathbf{r}. \quad (4)$$

From physical dimensionality of $P_I(0)$ it is tentative to introduce a quantity r_{cell} that has the meaning of a spatial scale, based on the following definition:

$$\sigma_{\text{cell}}^2 r_{\text{cell}}^2 = 4\pi^2 P_I(0) = \int_{\mathbb{R}^2} k_I(\mathbf{r}) d\mathbf{r} = 2\pi \int_0^{+\infty} k_I(r) r dr. \quad (5)$$

That is, $r_{\text{cell}} = 2\pi \sqrt{P_I(0)/k_I(0)}$. This r_{cell} will appear as one of key quantities below, so let us try to understand its physical meaning. Often it may serve as a measure of a cellularity scale in the random field, i.e. the typical size of a single correlation cell. However, counterexamples exist, in which the cellularity scale is different from r_{cell} . Let us now consider a few simple demonstrative cases.

(i) *White-noise field.* Let $P_I(s)$ is constant for $s < r_0^{-1}$ with some small r_0 , and zero otherwise. Then $k_I(r) = 2\sigma_{\text{cell}}^2 J_1(r/r_0) r_0/r$ and $r_{\text{cell}} = 2r_0\sqrt{\pi}$. In this case $k_I(r_{\text{cell}})/k_I(0) \approx 0.07$, meaning that brightness at two points separated by r_{cell} appears nearly uncorrelated, and hence such points likely belong to independent cells.

(ii) *Red-noise field.* Let $k_I(r) = \sigma_{\text{cell}}^2 e^{-r^2/(2r_0^2)}$. Then $P_I(s) = \sigma_{\text{cell}}^2 r_0^2 e^{-r_0^2 s^2/2}/(2\pi)$ and $r_{\text{cell}} = r_0\sqrt{2\pi}$. In this case $k_I(r_{\text{cell}})/k_I(0) \approx 0.04$, again a small correlation similar to the one from the first case.

(iii) *Blue-noise field.* Let $P_I(s) \propto s^2 e^{-r_0^2 s^2/2}$. Contrary to previous cases, this power spectrum is peaked at a non-zero s , close to r_0^{-1} , while $P_I(0) = 0$. The extra factor s^2 in this definition can be obtained by applying the

Laplace operator to k_I from the previous example, so after proper normalization it should be $k_I(r) = \sigma_{\text{cell}}^2 \kappa(r/r_0)$, where $\kappa(u) = (1 - u^2/2)e^{-u^2/2}$. This example has $r_{\text{cell}} = 0$ for any r_0 , so r_{cell} becomes non-physical. A reasonable measure of cellularity scale can be set to the same value as in the previous example, $r'_{\text{cell}} = r_0\sqrt{2\pi}$.

As we can see, r_{cell} describes the cellularity scale well if $k_I(r) \geq 0$ everywhere, but issues may appear if k_I is sign-changing. An alternative measure could be based on integrating $|k_I|$ or k_I^2 . But, for example, in the white-noise case the integral of $|k_I|$ is infinite, while the integral of k_I^2 yields exactly the same value, $r_{\text{cell}} = 2r_0\sqrt{\pi}$. Yet another way is to define the cellularity scale through the first zero of $k_I(r)$, which is $r = 1.08r_{\text{cell}}$ for the white noise, but this definition does not work if $k_I \geq 0$. In general, it appears not so easy to construct a universally good measure of cellularity scale, but our r_{cell} often retains this meaning (and even for sign-changing k_I cases).

Several simulated examples of our toy models are shown in Fig. 3. These random fields were generated on a grid of 120×120 pixels and take into account the spherical curvature of stellar surface. This was achieved by setting the argument of $k_I(r)$ to $r = 2\sin \frac{\alpha}{2}$, where α is the angle between two 3D unit vectors \mathbf{w} and \mathbf{w}' determining positions on a sphere with $R_* = 1$. The components w_x and w_y represented image coordinates, while w_z was derived as $w_z = \sqrt{1 - w_x^2 - w_y^2}$. In such a way we constructed the full covariance matrix for all 14400 image points, and then simulated the PBF image as a multivariate Gaussian vector.²

The images were also post-modulated by a quadratic limb-darkening law ($A = 0.4, B = 0.2$). All plots correspond to the same value of the relative quantity $\varepsilon_{\text{cell}} = \sigma_{\text{cell}}/I_0 = 0.1$, where I_0 is the nominal brightness at the disc center. The value of r_{cell} is labelled in each plot (it is assumed relative to R_*).

For each simulated PBF we then computed (numerically) a transit signal for a potential planet with $r_{\text{pl}} = R_{\text{pl}}/R_* = 0.15$. These transit curves are shown in the bottom part of Fig. 3. We can see that they reveal a randomly varying perturbation, owed to photospheric inhomogeneities. Our further goal is to determine the statistical properties of this perturbation, based on the $k_I(r)$.

In case of the Sun, the spatial power spectrum of its photospheric brightness field was investigated decades ago, see e.g. Karpinskii & Mekhanikov (1977). In terms of our $P_I(s)$, this spectrum remains more or less constant down to the granulation scale ~ 1000 km, where it starts to quickly decrease. Therefore, solar surface should better correspond to the white-noise example above (though its granularity is more fine than shown in any PBF of Fig. 3). However, this likely refers to only inactive photospheric domains, the effect of multiple spots on P_I is not very clear.

² The transition from Cartesian to spherical random field is unobvious in what concerns large-scale correlations. A more straightforward choice would be to set r proportional to the arc α , but this frequently generated a nonphysical covariance matrix (not strictly positive definite). The chord-based version, $r \propto \sin \frac{\alpha}{2}$, empirically allowed to bypass this issue. An entirely strict approach should likely involve spherical harmonics, but this is unnecessary for our sample simulations.

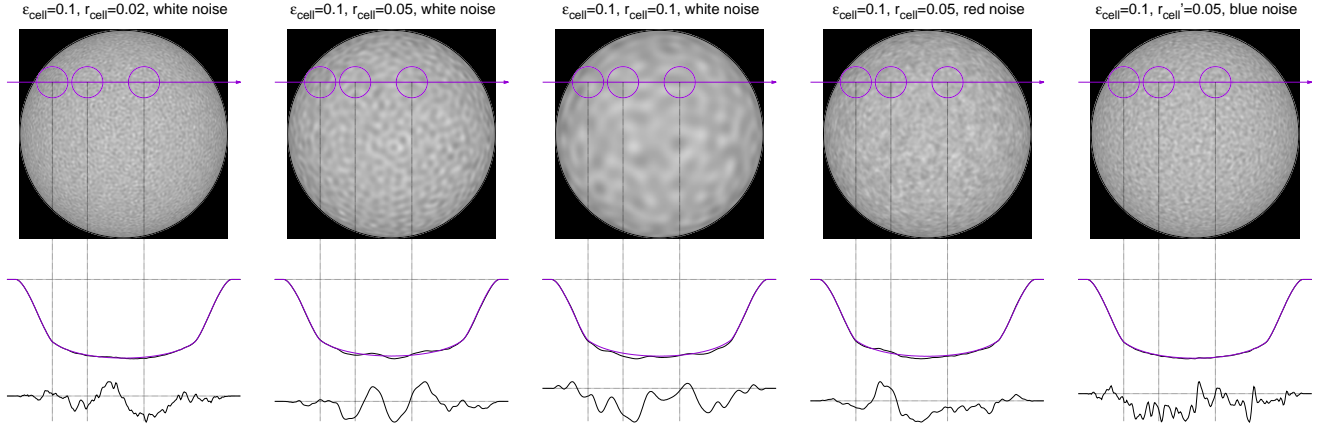


Figure 3. Modelling the stellar PBF: the simulated photosphere image (top row), the resulting transit signal (middle row), and the implied perturbation magnified (bottom row). The transiting planet has the radius of $0.15R_\star$, the transit impact parameter is $b = 0.5$, and the limb darkening coefficients are $A = 0.4$ and $B = 0.2$. See text for more details.

Notice that we do not assume here any particular correlation function k_I or the power spectrum $P_I(s)$, as our approach will not require to specify them in full. The simulated images in Fig. 3 are just examples, and we can construct different patterns by augmenting $P_I(s)$ with a more complicated behaviour. For example, it is possible to control the internal structure of a cell. Granulation pattern would require cells with a wider core and thin boundaries, while a spotted pattern may need smaller cell cores separated by relatively wider space. Such fine-tuning would require a more clever construction of $P_I(s)$ in the high- s range, but should not affect its low- s behaviour.

4 CHARACTERIZING THE TRANSIT PERTURBATION SIGNAL

Based on the PBF perturbation δI , let us write down the subplanet flux perturbation as

$$\delta F(\mathbf{x}) = \int p(\mathbf{x}' - \mathbf{x}) \delta I(\mathbf{x}') d\mathbf{x}', \quad (6)$$

where $p(\mathbf{r})$ is the indicator function of the projected planetary disc (unit for $r < r_{pl}$, and zero otherwise), \mathbf{x} is the position of planet center. As before, we assume $R_\star = 1$.

To understand the issue better, let us first consider a simplified case when x and x' are small (near the star disc centre), and therefore k_I is shift-invariable. Then the correlation function of δF is also shift-invariable and it can be expressed through a convolution:

$$\begin{aligned} k_F(\mathbf{x} - \mathbf{x}') &= \mathbb{E}(\delta F(\mathbf{x}) \delta F(\mathbf{x}')) \\ &= \iint p(\mathbf{x}'' - \mathbf{x}) p(\mathbf{x}''' - \mathbf{x}') k_I(\mathbf{x}'' - \mathbf{x}''') d\mathbf{x}'' d\mathbf{x}''' \\ &= \iint p(\mathbf{x}'' - \mathbf{x}) p(\mathbf{x}'' - \mathbf{x}' - \mathbf{r}) k_I(\mathbf{r}) d\mathbf{x}'' d\mathbf{r} \\ &= \int k_p(\mathbf{r} + \mathbf{x}' - \mathbf{x}) k_I(\mathbf{r}) d\mathbf{r} = (k_I * k_p)(\mathbf{x} - \mathbf{x}'), \\ k_p(\mathbf{r}) &= \int p(\mathbf{x}) p(\mathbf{x} - \mathbf{r}) d\mathbf{x} = (p * p)(\mathbf{r}). \end{aligned} \quad (7)$$

Therefore, $k_F(r)$ can be viewed as the “geometric kernel”

$k_p(r)$, blurred by $k_I(r)$, and all functions appear radially symmetric.

Notice that $k_p(r)$ equals to the intersection area beneath two circles, with radii r_{pl} both and with centers separated by r . Simple geometric constructions yield

$$k_p(r) = r_{pl}^2 \kappa\left(\frac{r}{r_{pl}}\right), \quad \kappa(u) = 2 \arccos \frac{u}{2} - u \sqrt{1 - \frac{u^2}{4}}. \quad (8)$$

We do not aim to adopt any specific k_I here. However, we need to make a no-so-restrictive assumption that k_I has a narrow localization, much smaller than r_{pl} . In this case, the convolution $k_p * k_I$ should impose only a negligible smoothing effect on k_p , regardless of the particular shape of k_I . Then slowly varying k_p can be moved out of the integration in (7):

$$k_F(r) \simeq k_p(r) \int k_I(\mathbf{r}') d\mathbf{r}' = k_p(r) \sigma_{cell}^2 r_{cell}^2. \quad (9)$$

Therefore, the effect of k_I is approximately equivalent to multiplying by a constant.

Now let us consider this effect in the Fourier space. The spatial power spectra obey, in turn, the multiplication law:

$$P_F(s) = P_I(s) P_p(s). \quad (10)$$

According to our assumption, k_I is narrow localized relative to k_p , hence the power spectra P_I and P_p should obey the opposite relationship. Therefore, regardless of a particular shape of P_I , we can replace $P_I(s)$ by $P_I(0)$ in (10), and this leads us to an equivalent multiplication by a constant.

Therefore, neglecting the projection effects, the correlation function $k_F(r)$ should be close to $k_p(r)$. A graph of this function is shown in Fig. 4. Its shape is close to a triangle, with the localization range $[-2r_{pl}, 2r_{pl}]$.

Now we should extend our approach to general conditions, involving near-limb projection. Then the PBF becomes not shift-invariable because of spherical curvature of the photosphere, hence k_I becomes a function of two arguments. We can generalize (7) as follows:

$$\begin{aligned} k_F(\mathbf{x}, \mathbf{x}') &= \mathbb{E}(\delta F(\mathbf{x}) \delta F(\mathbf{x}')) \\ &= \iint p(\mathbf{x}'' - \mathbf{x}) p(\mathbf{x}''' - \mathbf{x}') k_I(\mathbf{x}'', \mathbf{x}''') d\mathbf{x}'' d\mathbf{x}'''. \end{aligned} \quad (11)$$

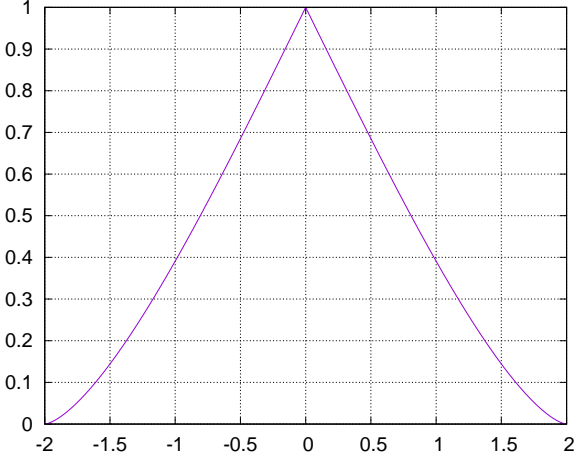


Figure 4. Correlation function $k_p(r)$, in normalized axes.

As before, we assume that k_I has narrow localization in comparison with p , meaning that we may equate $x'' = x'''$ everywhere in the integrand, except k_I itself:

$$k_F(\mathbf{x}, \mathbf{x}') = \int p(\mathbf{x}'' - \mathbf{x})p(\mathbf{x}'' - \mathbf{x}')d\mathbf{x}'' \int k_I(\mathbf{x}'', \mathbf{x}''')d\mathbf{x}'''. \quad (12)$$

In the shift-invariable case, the inner integral in (12) was equal to the constant $\sigma_{\text{cell}}^2 r_{\text{cell}}^2$, but now it is not so simple and may depend on \mathbf{x}'' . We need to dig into the properties of k_I to treat this dependence, so let us consider some effects that affect k_I and this integral.

(i) Considering an arbitrary sky-projected position \mathbf{x}'' in (12), the projection angle θ would be defined from $x'' = \sin \theta$. This projection effect anisotropically compresses the PBF pattern by the factor $\cos \theta$ in radial direction. However, $\cos \theta$ may vary only negligibly inside a single correlation cell. Hence, k_I can be treated shift-invariable in the local sense. Inside its localization domain, i.e. for \mathbf{x}''' within an $\sim r_{\text{cell}}$ distance from \mathbf{x}'' , we may assume that k_I depends on just the difference $\mathbf{x}'' - \mathbf{x}'''$. This dependence becomes anisotropic though. In turn, the inner integral in (12) should be reduced by the factor $\cos \theta$ because of the radial scale compression. That is, the integral should be amended to $\sigma_{\text{cell}}^2 r_{\text{cell}}^2 \cos \theta$, where $\cos \theta = \sqrt{1 - x''^2}$.

(ii) The limb darkening scales the apparent brightness according to a certain law, $I = I_{\text{ld}}(\mathbf{x})$, and we assume that it scales the perturbation field δI analogously. As long as k_I depends on δI in a quadratic manner, the inner integral in (12) should involve an additional factor $I_{\text{ld}}^2(\mathbf{x}'')/I_0^2$. Notice that we assume a quadratic limb darkening model, $I_{\text{ld}}/I_0 = Q(\cos \theta) = 1 - A(1 - \cos \theta) - B(1 - \cos \theta)^2$.

Combining these two conclusions together, we have

$$\int k_I(\mathbf{x}'', \mathbf{x}''')d\mathbf{x}''' \simeq \sigma_{\text{cell}}^2 r_{\text{cell}}^2 Q^2(\cos \theta) \cos \theta, \quad (13)$$

and (12) turns into

$$k_F(\mathbf{x}, \mathbf{x}') \simeq \sigma_{\text{cell}}^2 r_{\text{cell}}^2 \int p(\mathbf{x}'' - \mathbf{x})p(\mathbf{x}'' - \mathbf{x}')Q^2(\cos \theta) \cos \theta d\mathbf{x}''. \quad (14)$$

This formula can be rewritten as follows:

$$\frac{k_F(\mathbf{x}, \mathbf{x}')}{F_\star^2} = \kappa^2 k_{\text{pert}}(\mathbf{x}, \mathbf{x}'), \quad (15)$$

where

$$\kappa = \varepsilon_{\text{cell}} r_{\text{cell}} = 2\pi \frac{\sqrt{P_I(0)}}{I_0}, \quad (16)$$

and

$$k_{\text{pert}}(\mathbf{x}, \mathbf{x}') = \frac{I_0^2}{F_\star^2} \int p(\mathbf{x}'' - \mathbf{x})p(\mathbf{x}'' - \mathbf{x}')Q^2(\cos \theta) \cos \theta d\mathbf{x}'', \quad (17)$$

$$\frac{F_\star}{I_0} = \pi \left(1 - \frac{A}{3} - \frac{B}{6} \right),$$

with F_\star being the full out-of-transit flux from the star.

In the left part of (15) we have, in fact, the correlation function of $\delta F/F_\star$. It describes the relative flux change typically dealt with in transit fitting. In the right part we have the adimensional k_{pert} function scaled by κ^2 (also adimensional). While k_{pert} is computed from (17) entirely theoretically, the factor κ is a physical parameter characterizing the photospheric cellular pattern. This is the only characteristic left from k_I .

The integral in (17) contains rather simple well defined quantities, so it is clear in principle. It can be viewed as a more complicated version of some integrals that appear when computing the transit curve (Abubekurov & Gostev 2013) and the Rossiter-McLaughlin effect (Baluev & Shaidulin 2015). For example, the transit signal (or the relative in-transit flux drop) can be expressed as

$$\frac{\Delta F(\mathbf{x})}{F_\star} = \frac{I_0}{F_\star} \int p(\mathbf{x}'' - \mathbf{x})Q(\cos \theta)d\mathbf{x}'', \quad (18)$$

which has a similar structure as (17). It appears that our k_{pert} can be computed analogously, by expressing it through incomplete elliptic integrals. Unfortunately, this derivation appeared huge, as well as the final result. Moreover, at some levels it involved multiple conditional branches that are easy to implement algorithmically, but not so convenient to write down mathematically. In the online-only supplement we provide a C++ code that can compute $k_{\text{pert}}(\mathbf{x}, \mathbf{x}')$.

Though the derivation of k_{pert} appeared complicated, its graphical view is pretty simple. It is shown in Fig. 5. We can see that the variance of the perturbation expectedly decreases when planet moves from the central transit phase to a star limb. The correlation function in the middle of the transit appears similar to the triangular shape shown in Fig. 4, but in the ingress or egress phases it becomes more narrow.

Also, in Fig. 6 we present several simulated examples of the perturbation with correlation function from Fig. 5. Comparing them with the perturbation curves shown in Fig. 3, we may notice that they are generally similar, except that perturbations in Fig. 3 become more smooth for larger r_{cell} . This is an expected degradation of our approach accuracy, appearing if k_I becomes wider localized.

Our approximation of k_F may become invalid or inaccurate in three cases: (i) if k_I is not localized well enough, for example if r_{cell} exceeds r_{pl} , and (ii) if r_{cell} turns zero, like in the blue-noise field considered above, and (iii) if the PBF exhibits significant temporal variation.

The first case simply means that our approach may

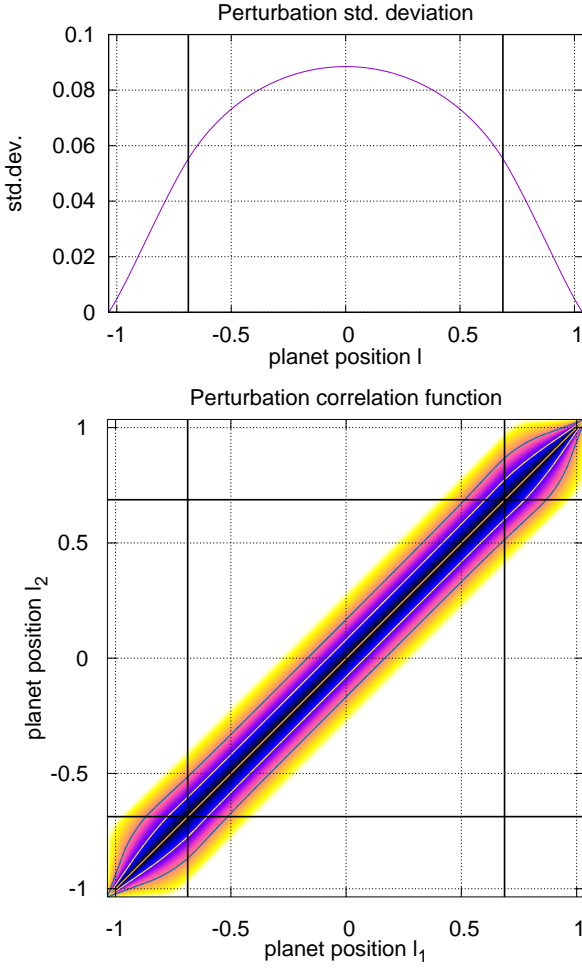


Figure 5. Top: Standard deviation $\sqrt{k_{\text{pert}}(\mathbf{x}, \mathbf{x})}$ as function of the transiting planet position. Bottom: The normalized correlation function $k_{\text{pert}}(\mathbf{x}, \mathbf{x}') / \sqrt{k_{\text{pert}}(\mathbf{x}, \mathbf{x})k_{\text{pert}}(\mathbf{x}', \mathbf{x})}$ as function of two independent positions of transiting planet. The planet and star parameters, and geometry of the transit, are the same as in Fig. 3. Quantity l (or $l_{1,2}$) stand for the planet 1D position along its transit path. Additional thick lines in the graphs label positions of the second and third contact.

not work well with large-scale PBF patterns that exceeds the planet size. In the second case, our primary approximation term (9,14) vanishes because of the degeneracy, and the shape of k_F is determined by higher order terms that we neglected. However, the magnitude of photometric perturbation should then become much smaller. Hence, PBFs of this type cannot generate large photometric perturbation, so in the context of our analysis there is no practical need to model them accurately. The third limitation appears if the PBF variation timescale becomes smaller than the correlation timescale of k_{pert} , which is equal to the time that planet needs to pass its diameter (designate it $2\tau_{\text{pl}}$). Solar granulation has ~ 10 min changing timescale (Nesis et al. 2002), and this appears comparable to $2\tau_{\text{pl}}$ for a typical hot Jupiter. Then the correlation wings of k_{pert} should be additionally suppressed by some PBF temporal stability function, effectively reducing the correlation timescale. However, even in

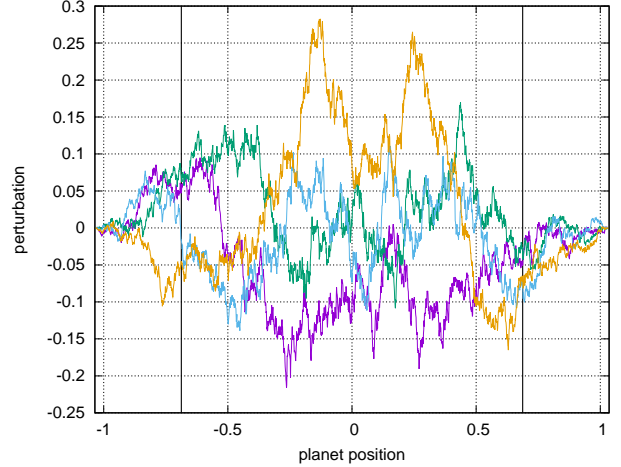


Figure 6. Several simulated examples of a Gaussian process that obeys the correlation function from Fig. 5. Two additional thick lines label positions of the second and third contact.

such a case this effect looks minor or moderate, at most. Moreover, Solar-type granulation has $\kappa \lesssim 10^{-3}$ and, as we will see below, such a signal does not seem detectable in TTV data like those we have for HD 189733, while possible PBF pattern for this target should have a much larger scale, and hence to be more stable temporally.

5 THE PBF EFFECT ON TRANSIT FITS

In terms of the magnitude, rather than flux, the perturbation signal is $\delta m \simeq 1.086 \delta F / F_*$. Therefore, the correlation function for the magnitude is $k_m \simeq 1.086^2 k_F / F_*^2$. From the other side, using (15) we have

$$k_m(\mathbf{x}, \mathbf{x}') = h k_{\text{pert}}(\mathbf{x}, \mathbf{x}'), \quad h = (1.086\kappa)^2, \quad (19)$$

where the sky-projected planet positions \mathbf{x} or \mathbf{x}' depend on the observation time t, t' in a deterministic way.

For any discrete set of observations we can build up the perturbation vector $\delta \mathbf{m} = \{\delta m(t_i)\}_{i=1}^N$, and then construct its $N \times N$ covariance matrix in the following form:

$$\mathbf{K}_m = h \mathbf{K}_{\text{pert}}, \quad (\mathbf{K}_{\text{pert}})_{ij} = k_{\text{pert}}(\mathbf{x}(t_i), \mathbf{x}(t_j)) \delta_{n_i n_j}, \quad (20)$$

where n_i and n_j are ordinal transit numbers which the observations i and j belong to, and $\delta_{n_i n_j}$ is their Kronecker delta (it forces zero correlation between different transits).

Basically, the perturbation $\delta \mathbf{m}$ can be viewed as an extra correlated noise that contaminates our lightcurve. Not only it is correlated, but also nonstationary. This perturbation will introduce biases to our lightcurve fit, in particular biases to the photometric noise model. This would not be a big issue, if this noise model could provide an accurate treatment for the perturbation. However, we typically use stationary noise models in practice. In such a case primarily the central part of the transit would be fitted well, but not the ingress/egress ranges, where the perturbation behaves differently (e.g. it has a smaller magnitude and is more short-scale correlated). On the other hand, timings depend more on the ingress/egress phases. Hence, a systematic distortion can be expected in them, and our further goal is to characterize it.

Let us consider this task in general. After all, we always use some method of fitting, i.e. a recipe how to construct the best fitting estimate $\hat{\xi}$ for a vector of free parameters ξ . Also, the method should yield some matrix $\hat{\Xi}$ as an estimate for the covariance matrix $\text{Var} \hat{\xi}$.³ Therefore, both $\hat{\xi}$ and $\hat{\Xi}$ are some functions of the input data \mathbf{m} , and they would change if \mathbf{m} is replaced by $\mathbf{m}' = \mathbf{m} + \delta\mathbf{m}$. In the second-order approximation,

$$\begin{aligned}\delta\hat{\xi}_i &= \hat{\xi}'_i - \hat{\xi}_i \simeq \sum_k \frac{\partial \hat{\xi}_i}{\partial m_k} \delta m_k + \frac{1}{2} \sum_{k,l} \frac{\partial^2 \hat{\xi}_i}{\partial m_k \partial m_l} \delta m_k \delta m_l, \\ \delta\hat{\Xi}_{ij} &= \hat{\Xi}'_{ij} - \hat{\Xi}_{ij} \simeq \sum_k \frac{\partial \hat{\Xi}_{ij}}{\partial m_k} \delta m_k + \frac{1}{2} \sum_{k,l} \frac{\partial^2 \hat{\Xi}_{ij}}{\partial m_k \partial m_l} \delta m_k \delta m_l.\end{aligned}\quad (21)$$

By our input conditions, $\mathbb{E}\delta m_k = 0$ and $\mathbb{E}\delta m_k \delta m_l = h(K_{\text{pert}})_{kl}$. Therefore, the biases in $\hat{\xi}$ and $\hat{\Xi}$ are:

$$\begin{aligned}\mathbb{E}\delta\hat{\xi} &\simeq h\Xi_{\text{bias}}, \quad (\Xi_{\text{bias}})_i = \frac{1}{2} \sum_{k,l} \frac{\partial^2 \hat{\xi}_i}{\partial m_k \partial m_l} (K_{\text{pert}})_{kl}, \\ \mathbb{E}\delta\hat{\Xi} &\simeq h\Xi_{\text{bias}}, \quad (\Xi_{\text{bias}})_{ij} = \frac{1}{2} \sum_{k,l} \frac{\partial^2 \hat{\Xi}_{ij}}{\partial m_k \partial m_l} (K_{\text{pert}})_{kl}.\end{aligned}\quad (22)$$

These biases reflect only a systematic part of a perturbation, while there is also random part for which we can compute the covariance matrix (for $\delta\hat{\xi}$), the 4-index covariance tensor (for $\delta\hat{\Xi}$), and the 3-index tensor for the cross-covariance between $\delta\hat{\xi}$ and $\delta\hat{\Xi}$. All these quantities can be approximated using only the linear terms of (21):

$$\begin{aligned}\text{Var} \delta\hat{\xi} &\simeq h\Xi_2, \quad (\Xi_2)_{ij} = \sum_{p,q} \frac{\partial \hat{\xi}_i}{\partial m_p} \frac{\partial \hat{\xi}_j}{\partial m_q} (K_{\text{pert}})_{pq}, \\ \text{Cov}(\delta\hat{\xi}, \delta\hat{\Xi}) &\simeq h\Xi_3, \quad (\Xi_3)_{i,j,k,l} = \sum_{p,q} \frac{\partial \hat{\xi}_i}{\partial m_p} \frac{\partial \hat{\Xi}_{kl}}{\partial m_q} (K_{\text{pert}})_{pq}, \\ \text{Var} \delta\hat{\Xi} &\simeq h\Xi_4, \quad (\Xi_4)_{ij,kl} = \sum_{p,q} \frac{\partial \hat{\Xi}_{ij}}{\partial m_p} \frac{\partial \hat{\Xi}_{kl}}{\partial m_q} (K_{\text{pert}})_{pq}.\end{aligned}\quad (23)$$

Perturbational characteristics defined in (22) and (23) are linear with respect to h and \mathbf{K}_{pert} . They in fact represent first terms of more general power series in h , so h should be small.

All these quantities can be computed analytically, though such a computation remains rather hard for the most. Nevertheless, we derive an analytic approximation for the most simple factor, Ξ_2 , because it involves only the gradient of $\hat{\xi}$. This derivation is layed out below.

First of all, we should specify the method of fitting as different methods may result in different quantities (22,23). We consider the maximum-likelihood Gaussian process fitting following from (Baluev 2013b) that was used in this work and in (Baluev et al. 2019). Our input data are the vector of photometric magnitudes \mathbf{m} , and they should be fitted as $\mathbf{m} = \mu(\theta) + \mathbf{n}$. Here $\mu(\theta)$ includes transit model and various deterministic trends, jointly parametrized by the lightcurve parameters θ . The noise vector \mathbf{n} follows a multivariate Gaussian distribution with the covariance matrix

³ Here we omit more complicated cases when the uncertainties are asymmetric and/or the error domains are nonelliptic.

$\text{Var} \mathbf{n} = \mathbf{V}(\eta)$ that depends on another set of parameters η (the noise parameters). That vector η usually includes variances of the red and white photometric noise treated as fittable quantities, and the red noise correlation timescales. The joint vector of free parameters is a combination of these two parametric sets, $\xi = \{\theta, \eta\}$.

The likelihood function of this task, in a classic definition, is given by

$$\log \mathcal{L}(\xi) = -\frac{1}{2} \log \det \mathbf{V} - \frac{1}{2} \mathbf{r}^T \mathbf{V}^{-1} \mathbf{r}, \quad \mathbf{r} = \mu - \mathbf{m}. \quad (24)$$

This function should be maximized to obtain the best fitting estimation of θ and η . However, following Baluev (2009), we typically amend this definition to

$$\log \tilde{\mathcal{L}}(\xi) = -\frac{1}{2} \log \det \mathbf{V} - \frac{1}{2\gamma} \mathbf{r}^T \mathbf{V}^{-1} \mathbf{r}, \quad \gamma = 1 - \frac{\dim \theta}{N}. \quad (25)$$

This modification allows to significantly reduce the bias in the noise parameters η that appears because the residuals \mathbf{r} represent, after the fitting, a systematically undervalued estimation of \mathbf{n} .

The best fitting estimation of ξ is given by the position of the maximum:

$$\hat{\xi} = \arg \max \tilde{\mathcal{L}}(\xi). \quad (26)$$

Mathematically, the necessary condition for the maximum is that gradient of $\log \tilde{\mathcal{L}}$ must vanish:

$$\left. \frac{\partial \log \tilde{\mathcal{L}}}{\partial \xi} \right|_{\xi=\hat{\xi}} = 0. \quad (27)$$

The covariance matrix of this $\hat{\xi}$ is then approximated as

$$\hat{\Xi} \simeq \mathbf{F}_{\hat{\xi}}^{-1}, \quad \mathbf{F}_{\hat{\xi}} = \begin{pmatrix} \mathbf{F}_{\theta} & \mathbf{0} \\ \mathbf{0} & \mathbf{F}_{\eta} \end{pmatrix}, \quad (28)$$

where \mathbf{F}_{ξ} is the Fisher information matrix for $\hat{\xi}$. Notice that it has a diagonal-block form with zero offdiagonal blocks, corresponding to the correlation between θ and η . Thanks to this, $\hat{\theta}$ and $\hat{\eta}$ are asymptotically uncorrelated for $N \rightarrow \infty$ (though some correlation may appear via higher-order terms in $1/N$). The expression for the θ -part of this matrix reads:

$$\mathbf{F}_{\theta} = \mathbf{Q} = \mathbf{J}^T \mathbf{V}^{-1} \mathbf{J}, \quad \mathbf{J} = \frac{\partial \mu}{\partial \theta}. \quad (29)$$

The expression for \mathbf{F}_{η} is not used here.

Now, let us alter the input data \mathbf{m} by adding a $\delta\mathbf{m}$ perturbation. The condition of the best fit (27) should be identically satisfied for any $\delta\mathbf{m}$. By differentiating (27) with respect to $\delta\mathbf{m}$, we obtain

$$\begin{aligned}\frac{\partial^2 \log \tilde{\mathcal{L}}}{\partial \xi \partial (\delta\mathbf{m})} + \frac{\partial^2 \log \tilde{\mathcal{L}}}{\partial \xi^2} \frac{\partial \hat{\xi}}{\partial (\delta\mathbf{m})} &= 0 \implies \\ \implies \frac{\partial \hat{\xi}}{\partial (\delta\mathbf{m})} &= \left(\frac{\partial^2 \log \tilde{\mathcal{L}}}{\partial \xi^2} \right)^{-1} \frac{\partial^2 \log \tilde{\mathcal{L}}}{\partial \xi \partial (\delta\mathbf{m})}.\end{aligned}\quad (30)$$

Based on the definitions (24,25), we can compute the following derivatives:

$$\frac{\partial \log \tilde{\mathcal{L}}}{\partial (\delta\mathbf{m})} = \frac{\mathbf{r}^T \mathbf{V}^{-1}}{\gamma} \implies \frac{\partial^2 \log \tilde{\mathcal{L}}}{\partial \theta \partial (\delta\mathbf{m})} = \frac{\mathbf{J}^T \mathbf{V}^{-1}}{\gamma}, \quad (31)$$

The Hessian $\partial^2 \log \tilde{\mathcal{L}} / \partial \xi^2$ is usually approximated when solving the optimization task (26). Its structure is similar to the negative- \mathbf{F}_{ξ} matrix, for example the θ -block can be

approximated by $-\mathbf{Q}/\gamma$. Therefore, plugging (29) and (31) into (30), we have

$$\frac{\partial \hat{\boldsymbol{\theta}}}{\partial(\delta \mathbf{m})} \simeq \mathbf{Q}^{-1} \mathbf{J}^T \mathbf{V}^{-1}, \quad (32)$$

while from (23) we obtain

$$\text{Var}(\delta \hat{\boldsymbol{\theta}}) \simeq h \boldsymbol{\Theta}_2, \quad \boldsymbol{\Theta}_2 = \mathbf{Q}^{-1} \mathbf{J}^T \mathbf{V}^{-1} \mathbf{K}_{\text{pert}} \mathbf{V}^{-1} \mathbf{J} \mathbf{Q}^{-1}. \quad (33)$$

This formula approximates the submatrix of Ξ_2 that corresponds to $\boldsymbol{\theta}$.

Concerning the other quantities from (22,23), we use Monte Carlo simulations to assess them. Given the basic best fit of our lightcurves set, we compute the matrix \mathbf{K}_{pert} and then generate Gaussian noise $\delta \mathbf{m}$ with zero mean and this covariance matrix. This simulated perturbation is scaled by $\sqrt{h^*}$ with some small *a priori* selected h^* , and then added to the input data which are then refit. Thus we derive a perturbed trial of $\hat{\boldsymbol{\xi}}$ and $\hat{\Xi}$, yielding the shifts $\delta \hat{\boldsymbol{\xi}}$ and $\delta \hat{\Xi}$. These shifts are averaged themselves or in pairwise products necessary to estimate all the quantities (22,23). Finally, the results are divided by h^* to extract the first-order factors. This yields the estimations for all five required entities: vector $\boldsymbol{\xi}_{\text{bias}}$, matrices Ξ_{bias} and Ξ_2 , tensors $\Xi_{3,4}$. The alternative analytic approximation (33) can be used for an additional validation of $\boldsymbol{\Theta}_2$, the submatrix of Ξ_2 .

6 INTERPRETING THE TTV NOISE OF HD 189733

Our goal in this section is to fit the transit timing data $\boldsymbol{\tau}$ with some simple model $\boldsymbol{\mu}(\mathbf{p})$, e.g. a linear trend with coefficients \mathbf{p} , and simultaneously via the noise parameter h . This will give us the understanding whether the TTV noise excess of HD 189733 can be modelled through our PBF model, and how physical this model is in relation with actual observations.

In our analysis we used the same 42 transit lightcurves selected in Sect. 2. They included ~ 7000 photometric measurements, and so the PBF perturbation is characterized by the covariance matrix \mathbf{K}_{pert} of $\sim 7000 \times 7000$ elements. Because of such a size, it cannot be presented here even in graphical form, but in the online-only material we supply a EPS file showing \mathbf{K}_{pert} as a 2D diagram. Correlations seen in this matrix appear either inside a single lightcurve, or between lightcurves that refer to the same transit.⁴

From now on, we deal with only a subsample of the fit parameters $\boldsymbol{\xi}$ that refer to the midtimes $\boldsymbol{\tau}$. A best fit results in the estimate $\hat{\boldsymbol{\tau}}$ and its covariance matrix estimate $\hat{\mathbf{T}}$ (which is sampled from $\hat{\Xi}$). Analogously to $\hat{\boldsymbol{\tau}}$ and $\hat{\mathbf{T}}$, we can sample subsets from the vector $\boldsymbol{\xi}_{\text{bias}}$, the matrices Ξ_{bias} , Ξ_2 , and the tensors $\Xi_{3,4}$, resulting in some $\boldsymbol{\tau}_{\text{bias}}$, \mathbf{T}_{bias} , \mathbf{T}_2 , and $\mathbf{T}_{3,4}$. We computed all these five entities for HD 189733 based on $h^* = 10^{-6}$ and 2.5×10^5 Monte Carlo trials. With so big number of trials, all Monte Carlo uncertainties were negligible.

Let us first consider some preliminary details of how this model works with HD 189733 data. This is necessary to

better understand what should be taken into account, and what can be neglected.

First of all, in the left-top panel of Fig. 7 we can see that timing measurements are very inhomogeneous regarding their uncertainties. Their accuracy vary from a few seconds to a few minutes, and this is why analysing such data is so difficult. The high-accuracy points contribute the largest information in a TTV fit, but simultaneously they should be more sensitive to various systematic perturbations. Here and in further plots we especially label four HST timings, because in (Baluev et al. 2021) it was noticed that these lightcurves do demonstrate some residual trends of unclear nature.

The meaning of the vector $\boldsymbol{\tau}_{\text{bias}}$ is easy. The PBF perturbation triggers a systematic bias in each transit timing, and these biases are approximated by $h \boldsymbol{\tau}_{\text{bias}}$. Notice, however, that we did not expect a bias of this type in Sect. 2. Basically, our PBF model reveals that TTV noise excess can be related with timing biases in a mathematically predictable way. The numeric values of individual $\boldsymbol{\tau}_{\text{bias}}$ elements for HD 189733 are shown in left-bottom panel of Fig. 7.

However, our primary effect is the increase of the apparent TTV noise through the matrix \mathbf{T}_2 . The most important information is carried in its diagonal elements that describe how the timing variances are affected. To characterize this effect, we introduce the following Uncertainty Response Coefficients as

$$\text{URC}_i = \sqrt{(T_2)_{ii}} \quad (34)$$

The quantity $\text{URC} \times \sqrt{h}$ has the meaning of the TTV “jitter” analogous to σ_{jit} from Sect. 2. However, now this jitter is not constant and depends on the timing.

Matrix \mathbf{T}_2 describes how the *true* covariance matrix is perturbed. But in actuality we deal with the estimate $\hat{\mathbf{T}}$ which is biased itself by $h \mathbf{T}_{\text{bias}}$. Hence this bias should be subtracted and the correction matrix \mathbf{T}_2 should be replaced with

$$\mathbf{T}_{\text{pert}} = \mathbf{T}_2 - \mathbf{T}_{\text{bias}}. \quad (35)$$

The URC definition (34) should be transformed to

$$\text{URC}'_i = \sqrt{|(T_{\text{pert}})_{ii}|}. \quad (36)$$

This quantity describes the “effective jitter” to be added to the *estimated* timing uncertainty that we actually deal with.

The values of URC and URC' for HD 189733 are shown in middle column of Fig. 7. We can see that these coefficients span rather wide numeric range, about two orders of magnitude, so the additive noise model with a constant jitter could not model the PBF effect correctly. Notice that \mathbf{T}_2 is positive definite, by definition, so its diagonal elements could be only positive. But \mathbf{T}_{pert} can be indefinite in general and may include positive as well as negative diagonal elements. That is, the PBF effect may systematically increase or systematically decrease the timing uncertainty. Negative occurrences mean that the corresponding uncertainty is expectedly overvalued because of the perturbation.

In Fig. 8 we also plot 2D diagrams related to several correlation matrices: the correlation matrix for $\boldsymbol{\tau}_i$, the correlation matrix corresponding to \mathbf{T}_2 , for its analytic and simulated approximations, and the diagonal-descaled (correlation-like) matrix for \mathbf{T}_{bias} . We plot only absolute values disregarding the signs. From these plots we can see

⁴ We assumed here that the perturbation signal is identically the same in such lightcurves. In actuality it may somewhat differ because of different bandpasses, but in this study we omitted possible effects of the bandpass dependence.

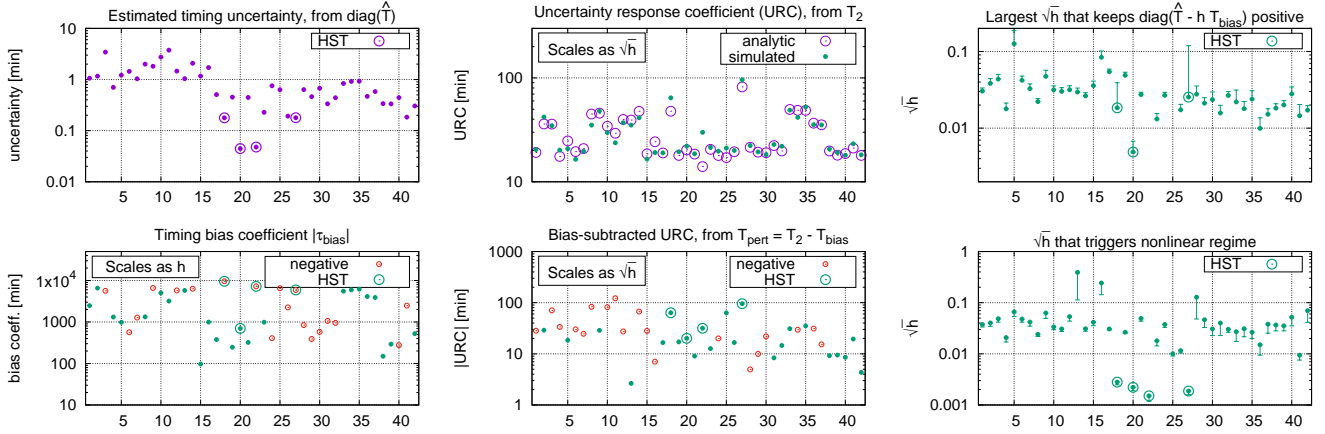


Figure 7. Several timing-related characteristics implied by the PBF model of HD 189733. See text for the explanation.

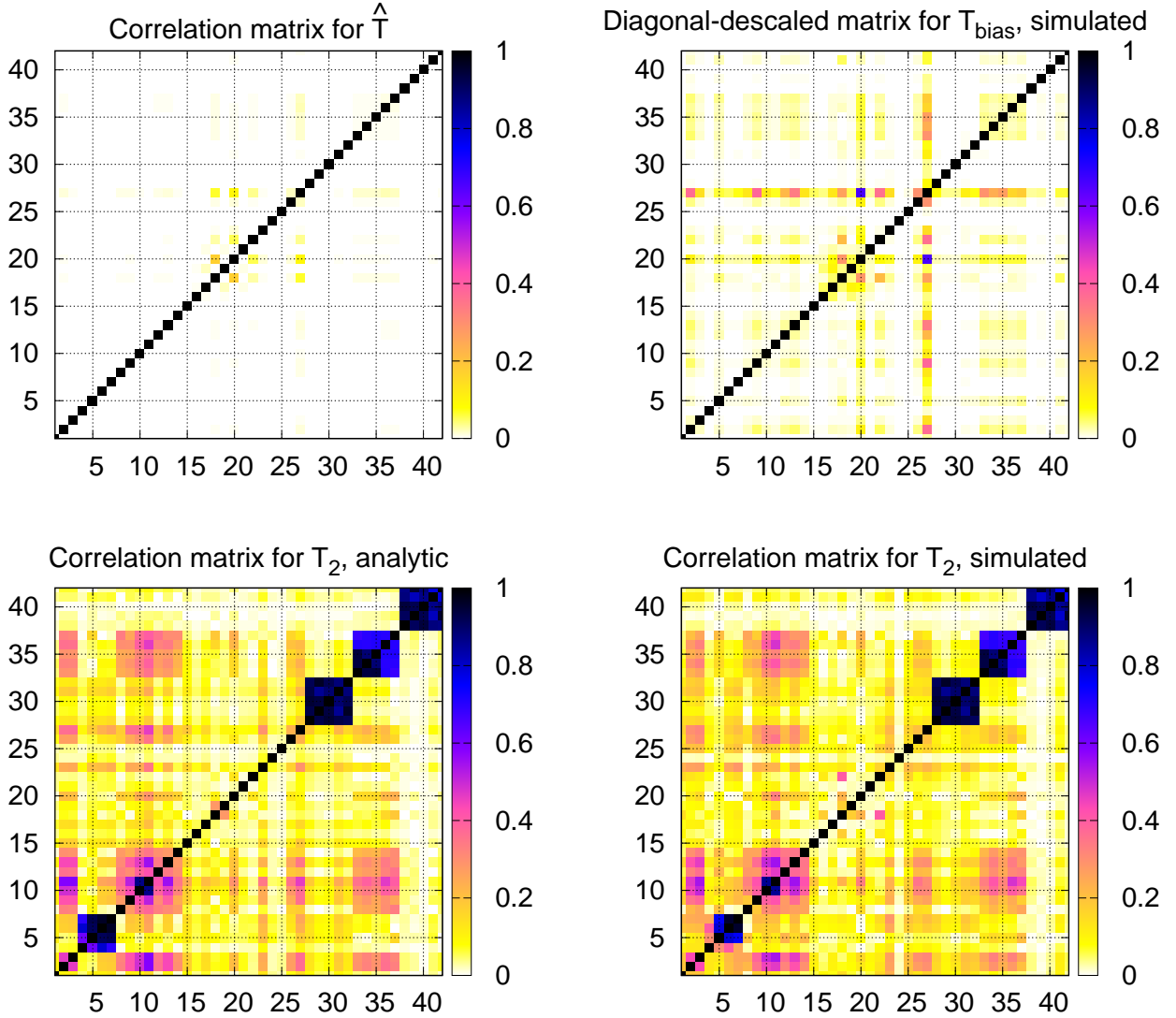


Figure 8. Correlation matrices implied by the PBF model of HD 189733. See text for the explanation.

that \mathbf{T}_2 may boost significant correlations between timings, even though such correlations are not seen in $\hat{\mathbf{T}}$. The effect from \mathbf{T}_{bias} on timing correlations is smaller. Also, from both Fig. 7 (middle-top panel) and Fig. 8 (two bottom panels) it follows that analytic and simulated versions of \mathbf{T}_2 are in good agreement with each other.

The further effect on timing uncertainties comes from the tensors $\mathbf{T}_{3,4}$ that describe random errors in $\hat{\mathbf{T}}$ owed to the PBF. However, their practical impact appeared more complicated, and before considering it we need to understand the applicability ranges for our TTV model. In view of that two additional characteristics can be considered, as defined below.

According to the physical meaning of \mathbf{T}_{bias} , the difference $\hat{\mathbf{T}} - h\mathbf{T}_{\text{bias}}$ represents the “unperturbed” covariance matrix of τ , i.e. the one that would appear without PBF perturbation. Therefore, $\hat{\mathbf{T}} - h\mathbf{T}_{\text{bias}}$ should necessarily be a positive definite matrix. In particular all its diagonal elements must be positive, otherwise such a model appears nonphysical. This restriction allows to derive an upper limit on h . This limit, however, can be somewhat relaxed because each $(\hat{T})_{ii}$ has a probable error about $\sqrt{h(T_4)_{iiii}}$. Assuming that $(\hat{T})_{ii}$ is undervalued by $s\sqrt{h(T_4)_{iiii}}$ with some factor s (number of sigma), the “unperturbed” variance should then be $(\hat{T})_{ii} + s\sqrt{h(T_4)_{iiii}} - h(T_{\text{bias}})_{ii}$. Requiring it to be positive results in an inequality that can be solved for \sqrt{h} , yielding an s -sigma upper boundary:

$$\sqrt{h} \leq \begin{cases} \frac{(\hat{T})_{ii} + s\sqrt{h(T_4)_{iiii}} - h(T_{\text{bias}})_{ii} \geq 0 \implies \sqrt{(T_4)_{iiii}} + \sqrt{(T_4)_{iiii} + 4(\hat{T})_{ii}(T_{\text{bias}})_{ii}}}{2(T_{\text{bias}})_{ii}}, & s = 1, \\ \sqrt{\frac{(\hat{T})_{ii}}{(T_{\text{bias}})_{ii}}}, & s = 0. \end{cases} \quad (37)$$

This requires $(T_{\text{bias}})_{ii} > 0$. If it turns negative for some i , the corresponding diagonal element in $\hat{\mathbf{T}} - h\mathbf{T}_{\text{bias}}$ keeps positive for any $h > 0$, and hence such transits set no limit on h .

In Fig. 7, right-top panel, we plot the boundaries (37) as points with one-sided errorbars. We can see that most of them reside above the level $h = 0.01$, except for a single HST observation. Therefore, $h \gtrsim 0.01$ or so renders our PBF model definitely non-physical (though it may remain formally tractable in mathematical sense). The range from $h \sim 0.005$ to $h \sim 0.01$ is somewhat disputable, because we have only a single point there. This may indicate, alternatively, that this particular HST lightcurve is odd in some sense (e.g. it may have an undervalued uncertainty owed to some overfit effect).

Another model limitation appears because we considered only linear effects in terms of h . This necessitates that all corrections to $\hat{\mathbf{T}}$ should remain small. The systematic correction to $(\hat{T})_{ii}$ is $h(T_{\text{pert}})_{ii}$, while the correction due to random errors is $\pm s\sqrt{h(T_4)_{iiii}}$. The maximum absolute correction should be kept small in comparison with $(\hat{T})_{ii}$, resulting in the following limits:

$$\sqrt{h} \gtrsim \begin{cases} h|(T_{\text{pert}})_{ii}| + s\sqrt{h(T_4)_{iiii}} \lesssim (\hat{T})_{ii} \implies \frac{\sqrt{(T_4)_{iiii} + 4(\hat{T})_{ii}|(T_{\text{pert}})_{ii}|} - \sqrt{(T_4)_{iiii}}}{2|(T_{\text{pert}})_{ii}|}, & s = 1, \\ \sqrt{\frac{(\hat{T})_{ii}}{|(T_{\text{pert}})_{ii}|}}, & s = 0. \end{cases} \quad (38)$$

The boundaries (38) are shown in the right-bottom panel of Fig. 7, again with one-sided errorbars. To keep our

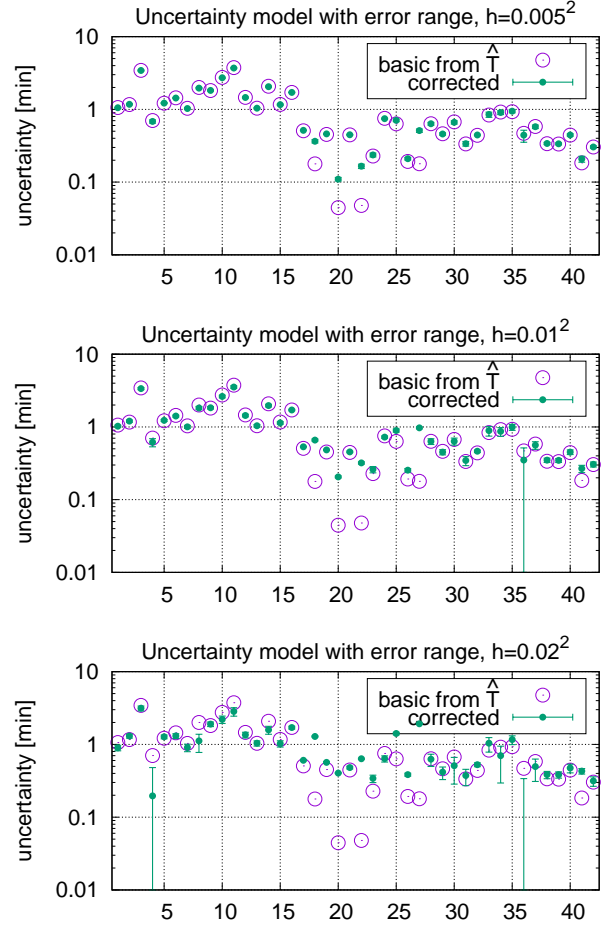


Figure 9. Corrected timing uncertainties implied by the PBF model of HD 189733, as derived from three reference values of the h parameter. Each uncertainty includes a error bar owed to the statistical nature of the PBF perturbation.

model mathematically accurate, h should stay below them. Larger h does not turn the model non-physical, but our linear approximation may appear inaccurate without higher-order terms in h . We can see that majority of the data imply the limit $h \lesssim 0.01$, just like previously. However, four HST points reside in the range $h \sim 0.001$ to $h \sim 0.003$. It is not entirely clear, whether these four points may corrupt our TTV analysis, but this range of h should be considered with care again.

Now let us return to the effect of random errors in $\hat{\mathbf{T}}$. They can make our task considerably more complicated from the analytic point of view, because the analysis should include some treatment regarding the “uncertainty of the uncertainty” phenomenon. This change may cause an increase of the complexity, but currently it is unclear how big this effect is and whether it should be taken into account. Now, when reasonable range for h is established, the easiest way to assess this effect is to compute it for practical data and a few sample h . This is presented in Fig. 9, where we show corrected timing uncertainties (from $\hat{\mathbf{T}} + h\mathbf{T}_{\text{pert}}$) and their potential errorbars (from $h\mathbf{T}_4$). We can see that nearly all errorbars remain negligible even for $h = 0.02$. For $h = 0.01$ just a single transit demonstrates a big errorbar, and for

$h = 0.005$ all errorbars are negligible. This enables us to conclude that the total effect from the covariance tensors $\mathbf{T}_{3,4}$ is likely not important in the context of these particular data of HD 189733. We can analyse these data using a more traditional approach with deterministic uncertainties.

To fit the TTV data honouring the remaining (non-random) corrections, we should subtract the bias $h\tau_{\text{bias}}$ from $\hat{\tau}$, and correct the covariance matrix $\hat{\mathbf{T}}$ by adding $h\mathbf{T}_{\text{pert}}$. Assuming that timing errors are Gaussian, the likelihood function becomes similar to (24):

$$\begin{aligned} \log \mathcal{L}_{\text{TTV}}(\mathbf{p}, h) &= -\frac{1}{2} \log \det \mathbf{T} - \frac{1}{2\gamma} \mathbf{r}^T \mathbf{T}^{-1} \mathbf{r}, \\ \mathbf{T} &= \hat{\mathbf{T}} + h\mathbf{T}_{\text{pert}}, \quad \mathbf{r} = \boldsymbol{\mu}(\mathbf{p}) - \hat{\tau} + h\tau_{\text{bias}}, \\ \gamma &= 1 - \frac{\dim \mathbf{p}}{N\tau}. \end{aligned} \quad (39)$$

The best fitting estimate is obtained by maximizing this \mathcal{L}_{TTV} with respect to h and \mathbf{p} . Notice that h is a mixed-type parameter, affecting both the TTV noise (through \mathbf{T}) and the TTV curve (through \mathbf{r}).

The results of these TTV fits for HD 189733 are presented in Table 3. We use two models for $\boldsymbol{\mu}(\mathbf{p})$: linear or quadratic trend. Our primary fits involve 42 timings selected in Sect. 2. In the context of the above-discussed TTV effects, Kasper et al. (2019) data do not reveal any odd behaviour, however the four HST timings do: they have especially low formal uncertainty, hence highest sensitivity to the PBF perturbation, and so inspire higher model nonlinearity. Besides, as noticed above, they may involve incompletely reduced photometric trends that may or may not be related to the hypothetical PBF effect. Therefore, we performed additional analysis for only 38 timings removing the HST ones.

From these results, we can make the following conclusions:

- (i) The goodness-of-fit measure of the new fits appears significantly worse than in Sect. 2. This suggests that PBF model can incorporate only a fraction of the observed TTV excess.
- (ii) The best fitting \varkappa parameter of the PBF model usually appears near its upper physical bound, that is the model tries to select the largest \varkappa still admissible. This again means that the model is largely deficient in explaining the TTV data.
- (iii) The formally fitted \varkappa corresponds, most closely, to the middle panel of Fig. 9. From this plot we can see that PBF perturbation mainly affects just the four timings coming from HST, and, possibly, a couple of others. Their initial formal uncertainties can be below 3 s, but should be boosted to, at least, ~ 10 s. From one side, this again confirms that HST lightcurves contain some perturbing trends, and our PBF model can make their uncertainties more adequate. However, the previously estimated TTV jitter from Table 1 appears much larger than 10 s, suggesting that we should also correct mid-accuracy timings, at least.
- (iv) A ‘forced’ increase of \varkappa too much above the ~ 0.01 level is impossible because some timing variances turn negative. This level defines the natural applicability limit for our PBF model and its maximum capabilities in how much it can explain the TTV jitter.

Because our PBF treatment keeps most of the uncertainties nearly intact, the formal significance of various pu-

tative TTV signals is greatly increased. For example, models with a quadratic TTV trend now have drastically larger likelihood than those with the linear one (they did not differ significantly in Sect. 2). The corresponding residual periodograms (see Fig. 10) also exceed formal significance level. It is still inobvious how trustable these periodograms can be, as their look is very model-dependent. But at least, from Table 3 it follows that by making the TTV signal more complicated the remaining TTV excess can be significantly reduced.

Therefore, the main conclusion from our analysis is that random PBF cannot explain the observed TTV jitter well. The largest admissible \varkappa can incorporate only a fraction of the observed TTV jitter, while further increase of \varkappa makes the model meaningless instead of generating a higher TTV noise.

On the other hand, our results do not reject the PBF effect for HD 189733. It can explain some part of the TTV jitter, at the maximum level of ~ 10 s. This is an important observational constraint on a physical effect that cannot be directly observed. In such a case, our estimation $\varkappa \simeq 0.01$ should be considered as an upper limit. If \varkappa was larger, for some transits we could not obtain so small timing uncertainties as we have, because their low limit is set by $h\tau_{\text{bias}}$. Notice that such \varkappa would correspond to the third plot of Fig. 3, for example.

7 DISCUSSION

In this work we designed a method to treat the impact of stellar photospheric field on exoplanetary transits. Our method does not assume any specific physical nature of brightness inhomogeneities and solves the task in a nearly model-invariable way. Namely, the PBF effect on the transit signal is proportional to just a single aggregate characteristic \varkappa , basically the PBF power spectrum taken at zero argument, $P_I(0)$. The correlation function of the photometric perturbation is universal and depends, in a mathematically defined way, only on the usual transit parameters and limb darkening. Therefore, the PBF perturbation can be fitted as a random process, through its scaling parameter \varkappa that has direct physical meaning.

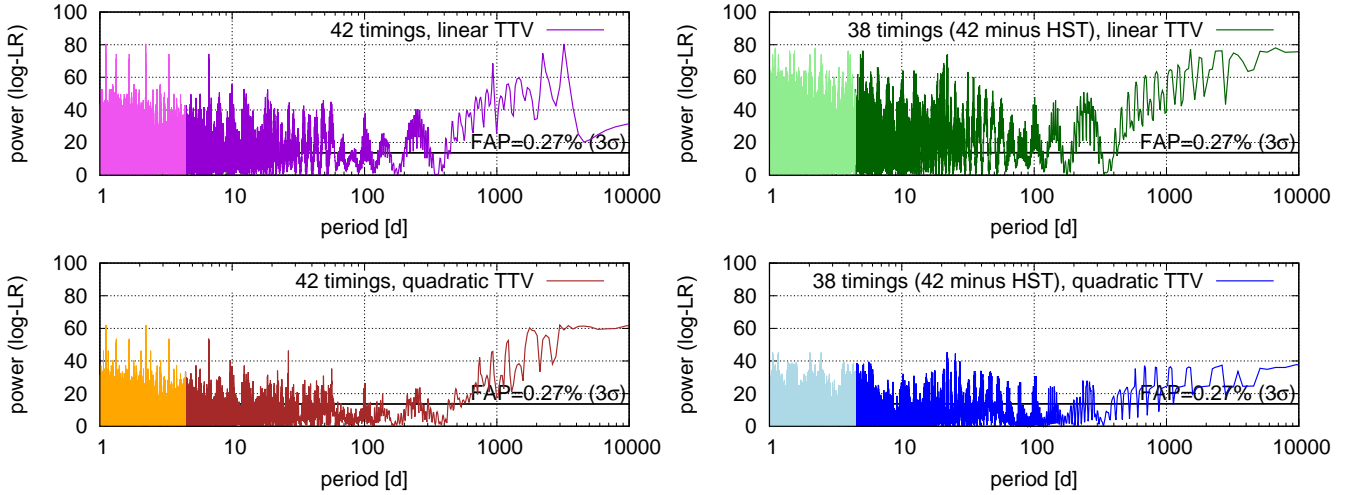
Summarizing all the investigations regarding HD 189733, the answer to our primary question, whether any photospheric brightness inhomogeneities can explain its TTV excess, is likely negative. The PBF effect cannot boost timings uncertainties consistently by more than ~ 10 s, while the actual TTV excess is ~ 70 s.

Therefore, the detailed source of TTV noise of HD 189733 remains unclear. It seems likely that there are multiple sources of this TTV noise that interfere in a complicated way. As discussed in Sect. 2, possible pipeline inaccuracies may undervalue derived timing uncertainties by $\sim 20\%$, but this again leaves most of TTV noise unexplained. It seems we should consider more seriously that some part of the TTV has a deterministic nature, e.g. a perturbation from another gravitating body. But because of complicated noise contamination we cannot characterize it well. Other possible sources that yet need a detailed investigation:

- (i) The effect of planetary atmosphere.

Table 3. TTV fits of the PBF model for HD 189733.

TTV model $\mu(p)$	Goodness-of-fit \tilde{l} [s]	$\kappa = \frac{\sqrt{\tilde{h}}}{1.086}$	Periodogram peak power
Initial set of 42 lightcurves:			
Linear	349.84	0.0090 ± 0.0012	80.4
Quadratic	215.77	0.0088 ± 0.0013	62.1
minus 4 HST lightcurves:			
Linear	436.70	0.0092 ± 0.0016	78.0
Quadratic	150.53	0.0066 ± 0.0023	45.4

**Figure 10.** Likelihood-based periodograms of HD 189733 timings, for the PBF fits from Table 3. Details are similar to Fig. 1.

(ii) Gravitational effect from hypothetical planets in a chaotic (but stable) dynamics, so that their TTV signal looks like noise.

(iii) Possible more complicated time-variable activity effects, e.g. related to the star magnetic activity cycle.

(iv) Incompletely compensated instrumental photometric drifts that occasionally contaminated some high-accuracy lightcurves.

(v) Some lightcurves may still involve erratic BJD/HJD correction (such cases do appear even in refereed papers, see Table 1 in [Baluev et al. 2021](#)).

Returning to the PBF effect and its modelling method that we developed, it is probably interesting to verify them with other planet hosts considered in ([Baluev et al. 2019](#)). Some of them also had a statistically significant TTV excess, though with a smaller magnitude than for HD 189733. The PBF model may appear more successful in such cases. However, the primary practical trouble with such analysis is the need of Monte Carlo simulations. Simulations are necessary to estimate all required corrections, in particular \mathbf{T}_{bias} and $\boldsymbol{\tau}_{\text{bias}}$. Our method involves analytic computation of \mathbf{T}_2 , and it demonstrated good agreement with simulations, but \mathbf{T}_{bias} and $\boldsymbol{\tau}_{\text{bias}}$ appeared too difficult for the analytic treatment. Resolving this issue can make the entire analysis pipeline drastically faster and more practical for a routine use.

ACKNOWLEDGMENTS

This work was supported by the Russian Science Foundation, project 19-72-10023. We highly appreciate fruitful comments and suggestions provided by the anonymous reviewer.

DATA AVAILABILITY

The data underlying this article are available in the article and in its online supplementary material.

REFERENCES

- Abubekrov M. K., Gostev N. Y., 2013, MNRAS, 432, 2216
- Agol E., Steffen J., Sari R., Clarkson W., 2005, MNRAS, 359, 567
- Bailey A., Goodman J., 2019, MNRAS, 482, 1872
- Bakos G. A., et al., 2006, ApJ, 650, 1160
- Baluev R. V., 2008, MNRAS, 385, 1279
- Baluev R. V., 2009, MNRAS, 393, 969
- Baluev R. V., 2012, MNRAS, 422, 2372
- Baluev R. V., 2013a, Astron. & Comput., 2, 18
- Baluev R. V., 2013b, MNRAS, 429, 2052
- Baluev R. V., 2015, MNRAS, 446, 1493
- Baluev R. V., 2018, Astron. & Comput., 25, 221
- Baluev R. V., Shaidulin V. S., 2015, MNRAS, 454, 4379
- Baluev R. V., et al., 2015, MNRAS, 450, 3101
- Baluev R. V., et al., 2019, MNRAS, 490, 1294
- Baluev R. V., et al., 2020, MNRAS, 496, L11
- Baluev R. V., et al., 2021, Acta Astron., 71, 25
- Boisse I., et al., 2009, A&A, 495, 959

- Bouma L. G., et al., 2019, *AJ*, 157, 217
- Bouma L. G., Winn J. N., Howard A. W., Howell S. B., Isaacson H., Knutson H., Matson R. A., 2020, *ApJ*, 893, L29
- Cauley P. W., Redfield S., Jensen A. G., 2017, *AJ*, 153, 217
- Chiavassa A., et al., 2017, *A&A*, 597, A94
- Claret A., Bloemen S., 2011, *A&A*, 529, A75
- Ford E. B., et al., 2011, *A&A*, 197, 2
- Holman M. J., Murray N. W., 2005, *Science*, 307, 1288
- Karpinskii V. N., Mekhanikov V. V., 1977, *Solar Physics*, 54, 25
- Kasper D. H., et al., 2019, *MNRAS*, 483, 3781
- Maciejewski G., et al., 2016, *A&A*, 588, L6
- Maciejewski G., et al., 2018, *Acta Astronomica*, 68, 371
- McCullough P. R., Crouzet N., Deming D., Madhusudhan N., 2014, *ApJ*, 791, 55
- Montalto M., Boué G., Oshagh M., Boisse I., Bruno G., Santos N. C., 2014, *MNRAS*, 444, 1721
- Nesis A., Hammer R., Roth M., Schleicher H., 2002, *A&A*, 396, 1003
- Pillitteri I., Wolk S. J., Lopez-Santiago J., Günther H. M., Sciortino S., Cohen O., Kashyap V., Drake J. J., 2014, *ApJ*, 785, 145
- Pont F., et al., 2007, *A&A*, 476, 1347
- Santos N. C., et al., 2013, *A&A*, 556, A150
- Sokov E. N., et al., 2018, *MNRAS*, 480, 291
- Steffen J. H., et al., 2013, *MNRAS*, 428, 1077
- Vuong Q. H., 1989, *Econometrica*, 57, 307
- Winn J. N., et al., 2007, *AJ*, 133, 1828
- Xie J.-W., 2013, *ApJS*, 208, 22

APPENDIX A: ONLINE MATERIAL

The paper contains the following online files:

- (i) ZIP archive with a C++ library that allows to compute the k_{pert} function.
- (ii) Scaleable EPS figure that shows full correlation matrix \mathbf{K}_{pert} computed for 42 transit lightcurves of HD 189733.

This paper has been typeset from a \LaTeX file prepared by the author.